

PAPER • OPEN ACCESS

High-speed digital light source photocurrent mapping system

To cite this article: Francesco Bausi *et al* 2019 *Meas. Sci. Technol.* **30** 095902

View the [article online](#) for updates and enhancements.

You may also like

- [Development of a multi-wavelength photocurrent mapping system](#)
G Berriman, B Routley, S Clothier et al.
- [Spatially resolved characterization of HgCdTe materials and devices by scanning laser microscopy](#)
J Bajaj, W E Tennant, R Zucca et al.
- [Does digital curriculum mapping improve curriculum alignment?](#)
I Khoerunnisa, I Widiaty, A G Abdullah et al.

High-speed digital light source photocurrent mapping system

Francesco Bausi¹, George Koutsourakis¹ , James C Blakesley¹ 
and Fernando A Castro¹ 

¹ National Physical Laboratory, Teddington TW11 0LW, United Kingdom

E-mail: fernando.castro@npl.co.uk

Received 27 February 2019, revised 12 April 2019

Accepted for publication 3 May 2019

Published 29 July 2019



Abstract

High-resolution spatial characterization of photovoltaic devices and photodetectors can reveal local defects that can have a detrimental impact on the lifetime and performance of such devices. Photocurrent mapping methods can provide high-resolution measurements and characterization can be achieved under actual operating conditions. However, such methods usually require costly, complicated systems and possess limited measurement speed. In this work an optical system based on a digital micro-mirror device is used for photocurrent mapping and a measurement protocol with a theoretical upper limit for scanning rate of 22 kHz is presented. The digital micromirror device itself provides synchronised spatial and temporal modulation in order to perform current mapping. Photocurrent maps of solar cells devices obtained with a scanning rate of 1000 pixels in less than 6 s are reported (the speed was limited by the device's response time and its photon to current conversion efficiency). The speed of photocurrent mapping is thus increased by almost two orders of magnitude compared to other methods and is only limited by the response of the device under test. A lateral resolution of 34 μm is achieved, with the potential to increase it even further. The absence of any moving parts allows high repeatability of measurements. Combined with the high-speed control of the light field, this enables the development of novel measurement techniques for the simultaneous measurement of temporal and spatial parameters. The fully digital control of the mapping system also presents a high potential for integration in industrial automated systems as it can be fully controlled using machine learning algorithms to achieve fast detection of crucial defects and features of devices during manufacturing.

Keywords: photovoltaics, photodetectors, current measurement, characterization, LBIC

(Some figures may appear in colour only in the online journal)

1. Introduction

Spatial variability of local parameters of photovoltaic devices and photodetectors can have a significant impact on their overall performance. The photocurrent density is not uniform across the illuminated area of such devices usually as a result of: inhomogeneous deposition procedures, local defects, specific design schemes or due to material properties. This can

have a crucial impact on the performance of PV modules [1] and photodetectors [2] therefore spatial characterisation of such devices is usually necessary to ensure product quality and reliable performance. Photocurrent mapping measurements can provide important information under actual operating conditions about the electrical, optical and material properties of a device.

Laser/light beam induced current (LBIC) measurements are commonly used to map the local current generation of PV devices and photodiodes [3, 4]. A typical implementation uses a focused light source and a point by point raster scan implemented with an x - y stage [5, 6] or a piezo-electric mirror

 Original content from this work may be used under the terms of the [Creative Commons Attribution 3.0 licence](https://creativecommons.org/licenses/by/3.0/). Any further distribution of this work must maintain attribution to the author(s) and the title of the work, journal citation and DOI.

[7, 8]. The photocurrent response is measured for every point of the measured area of a device, to generate a current map. Although high-resolution current mapping can be achieved, measurements are cumbersome and time consuming and LBIC systems can become rather expensive and complicated.

High-speed and high repeatability are prerequisites for developing reliable photocurrent mapping techniques for inline quality control in industrial production processes which could improve the quality of commercial devices. Recently, efforts have been demonstrated to achieve higher measurement speed using an LBIC system with the on-the-fly scanning approach. Measurements are performed via a continuously moving scanning beam resulting in a significant reduction of the measurement time, but on the other hand aberrations are introduced in the photocurrent map [9].

One of the most promising approaches to achieve higher scanning speeds and simplify measurement setups is using a digital micromirror device (DMD) [10]. The fast response of the DMD, in the μs scale, can lead to very fast current mapping systems. The use of a DMD has been successfully demonstrated in the past to obtain photocurrent maps of photovoltaic devices. However only a small fraction of its potential has been used so far for photocurrent mapping as the sampling rate was limited to less than ~ 10 pixels per second. Recently, the compressed sensing current mapping technique was introduced, utilising a DMD optical setup, for accelerating measurement acquisition [11, 12]. A camera enhanced system utilising compressed sensing for adaptive current mapping measurements has also been recently reported [13].

In this work a complete DMD-based photocurrent mapping system and a measurement protocol are presented. Synchronised with the measurement acquisition module, the DMD is not only performing the scan as in previous work, but it is also applying signal modulation in order to speed up measurement acquisition even further. A spatial resolution of $34 \mu\text{m}$ and scanning frequencies up to 22.727 kHz are achieved. Measurement of copper indium gallium selenide (CIGS) devices with a scanning speed of 1000 pixels in less than 6 s are reported here, which is an order of magnitude faster than conventional LBIC systems. The scanning speed is limited by the response time of the sample and by the speed of the current acquisition device. Smaller signals require a higher gain which results in slower sampling rate. The measurement protocol developed uses a lock-in amplification method which is implemented in post-processing which increases the signal-to-noise ratio (SNR) and drastically improves the trade-off between power and resolution typical of the DMD light modulation.

The system is compact and has no moving parts (except for the microelectromechanical parts in the DMD), which provides high repeatability of measurements achieving higher positioning accuracy than on-the-fly scanning methods, at also higher sampling speeds. Thanks to the unprecedented combination of speed and resolution the presented scanning approach could enable novel spatial-temporal characterisation techniques.

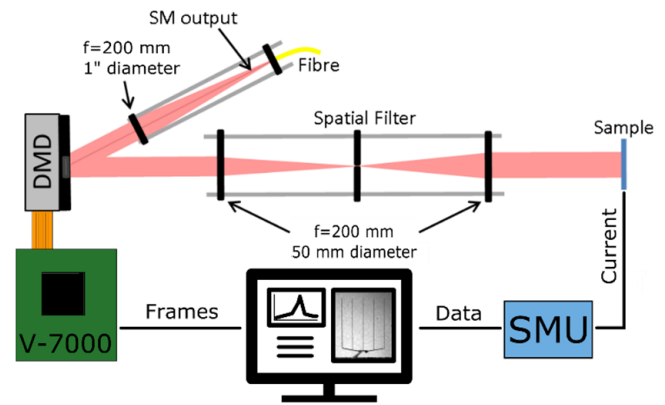


Figure 1. Schematic of the instrument setup.

2. Experimental setup

The schematic of the system is reported in figure 1 and is analytically described in [14]. The 70 mW output of a single-mode pig tailed 637 nm laser diode (Thorlabs LP637 SF70 driven with a Thorlabs LDC202C and temperature controller Thorlabs TED200C) is collimated through a 25.4 mm diameter convex lens with a focal length of 200 mm and overfills the DMD (ViALUX V-7000 module). The scanning beam is generated by controlling the DMD to shine a light-pattern with a defined profile on the sample. A source meter unit (SMU) was used to measure the photocurrent and also provide analog to digital conversion (see figure 1).

The DMD is composed of an array of 1024×768 mirrors. Each mirror has a size of $13.7 \mu\text{m}$ by $13.7 \mu\text{m}$ and can be tilted around a diagonal hinge by $\pm 12^\circ$ from its 'parked' (horizontal) position. This movement provides control of the direction of the reflected light. The relative positions of the mirrors are totally independent and the disposition of all mirrors in the frame can be refreshed up to 22 727 times a second (approximately once every $45 \mu\text{s}$) to display any desired pattern. By grouping different number of mirrors together, different pixel sizes and eventually different resolution scans can be acquired. For instance, by grouping squares of 100 mirrors together ($10 \text{ mirrors} \times 10 \text{ mirrors}$ squares), 100×100 pixel current maps can be acquired with a resolution of $137 \mu\text{m}$ for each pixel of the current map.

3. Digital light source

Due to the geometry of the optical system the DMD acts as a blazed diffraction grating [15]. The angle of incidence is adjusted using the Littrow conditions for the 5th order (30° incidence) in order to maximize the power transfer into a single diffraction order. The reflected beam is collimated using a 4f optical system and then projected onto the sample. A spatial filter (adjustable iris) is used at the Fourier plane to reduce blurring caused by the non-ideal alignment of the optics and thus increase the lateral resolution of the projected patterns. Higher order diffractions correspond to higher frequency features of the projection image, therefore blocking

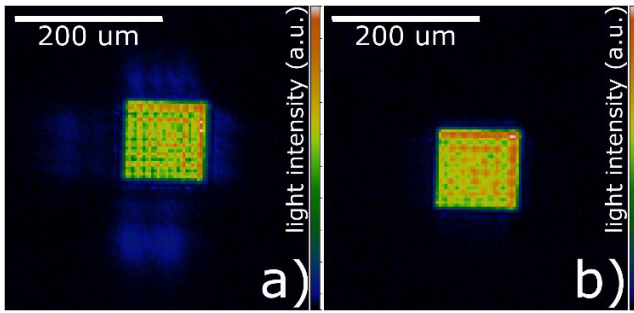


Figure 2. Beam profile at the sample plane for a 10×10 mirrors beam (a) and (b) obtained using a CMOS camera in place of the sample. The image (a) is produced with the spatial filter (iris) wide open whereas for the image (b) the iris was set to let only the first order of the beam's FT through. The unwanted components of the beam (deep blue) are filtered out using the spatial filter.

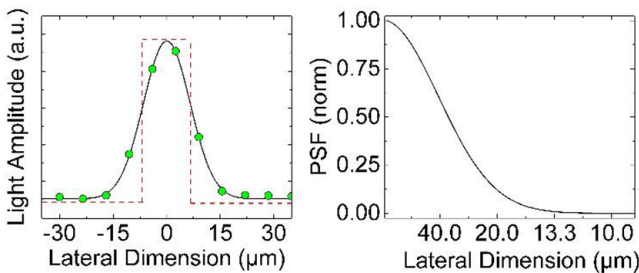


Figure 3. Profile of the light intensity produced by 1 micro-mirror at the sample plane using a spatial filter at the Fourier plane to block the higher order components (a) and the corresponding point spread function (b). The dashed line in (a) is the real size of the micro-mirror.

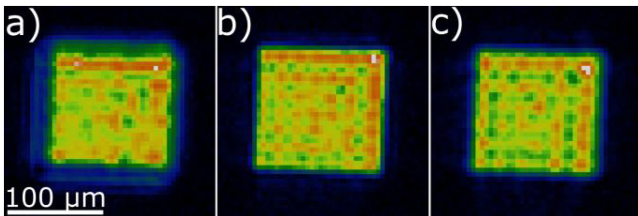


Figure 4. Focal depth of the projection around the focal plane (b). The images are acquired at 2 mm above (a) and below (c) the focal plane. The images were acquired using a CMOS camera so the intensity values are in arbitrary units.

them will also suppress the high frequency features of the projection as shown in figure 2, without nevertheless affecting the raster scanning process.

In figure 3(a) the profile of the light-pattern produced by a single mirror is fitted using a Gaussian distribution. The dashed line represents the size of the mirror. In figure 3(b) the point spread function (PSF) is shown as calculated from figure 3(a). The PSF represents the ability of an optical system to produce an image with finer details. The curve decreases to the 50% (cut-off) at a lateral resolution of $34 \mu\text{m}$ and this represents the maximum level of lateral resolution of the system.

The depth of field of the projection is relatively shallow $\sim \pm 1 \text{ mm}$, indicating the importance of good optical alignment. The z -axis position can be optimized by iteratively reducing the size of the features in the photocurrent maps. In

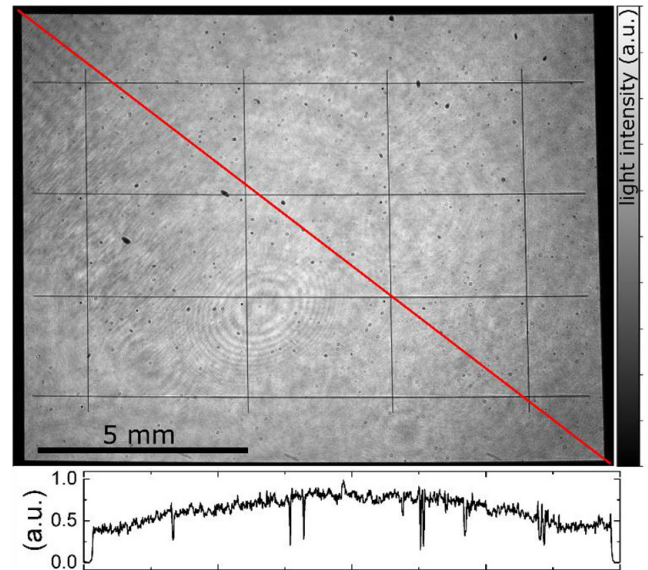


Figure 5. Relative intensity map of the entire DMD measured at the sample plane in arbitrary units (the image was acquired using a CMOS camera). The grid was produced by switching off specific single lines of mirrors. The graph shows the map profile along the red line. The other visible features are due to interference effects through the lenses or caused by dust particles on the optical path.

figure 4 the camera was shifted below and above the focal plane by only $\sim 2 \text{ mm}$ showing that the projected image becomes blurred due to the non-ideal alignment of the 4f optics.

The uniformity versus irradiance trade off is one of the main limitations of the current setup as can be seen in figure 5. The power at the corner of the light field is approximately 50% of the maximum. The uniformity can be improved at the expense of the irradiance by adding diffusion optics and re collimating the beam. Spatial homogeneity can be additionally improved by using a source with a larger spectral bandwidth. Nevertheless, the present non uniformity does not affect the scope of this work and will be improved in a future upgrade of the system. In the map of figure 5 some weak fringe patterns are also visible. Sources of such artefacts can be multiple reflections between lenses, diffraction of the lenses aperture and dust particles along the optical path.

The DMD allows the display of any arbitrary pattern of light on the sample surface. In this work a raster scanning method was used to map the photocurrent. To achieve this, adjacent square-shaped groups of mirror were consecutively turned on resulting in square-shaped beams flashing along a zig-zag path across the active area of the device under test. The mapping resolution (which was set equal to the size of the beam, i.e. square-shaped beams produced by adjacent groups of mirrors were successively turned on) is given by the number of mirrors along the edge of the square. Throughout the paper the groups of mirrors as described here are referred to as a 'pixel' whereas a single micro-mirror is usually referred to as a 'mirror'.

In figure 6 the transient irradiance during a pixel operation is shown. The laser beam reflected by a square pixel composed of 100 micro-mirrors (10 by 10 mirrors) was directed

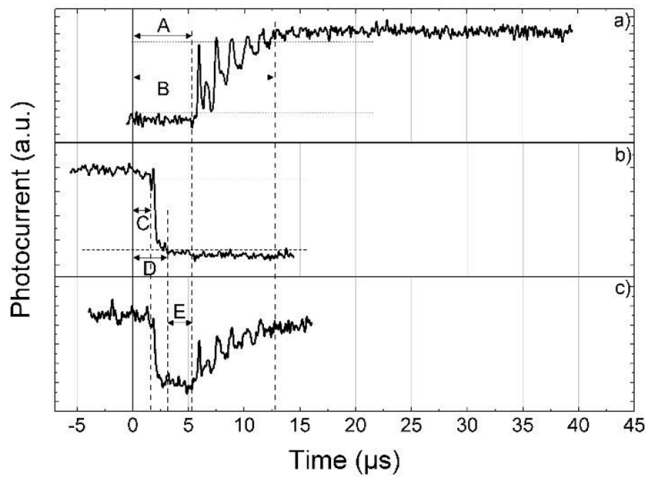


Figure 6. Photocurrent output of a 10×10 pixel during off-to-on (a), on-to-off (b) and on-to-on (c) transitions. Time is relative to the trigger pulse. The time duration for the main events in the various curves are labelled from (A) to (E) and are described as follows: (A) delay between a mirror tilting trigger and the relative beam entering the field of view of the photodiode, (B) time after which the beam’s oscillations are confined in the area of the photodiode, (C) time at which the beam starts to exit the area of the photodiode, (D) time it takes to the beam to exit the area of the photodiode completely, (E) time delay between the beam exiting the detector area and it entering in back in again. Please note that the times as shown in the curves are strongly dependent on the photodiode’s area and the number of pixels involved.

onto a biased silicon photodiode (Thorlabs DET10A). The current traces were measured using an oscilloscope (Tektronix DPO4000B).

In the off to on transition reported in figure 6(a) and in the on to on transition in figure 6(c) there is a delay of $\sim 5 \mu\text{s}$ between the trigger pulse ($t = 0 \mu\text{s}$) and the beam entering in the field of view of the photodiode to be detected movement of the mirrors. The spikes in the photocurrent during the transition are most likely due to the dampened oscillations of the mirrors around the new position. A reset step is completed within the first $\sim 3 \mu\text{s}$ before the beam is deflected out of the active area of the photodiode as the mirrors are set to their new position as can be seen in figures 6(b) and (c). The on to off transition (fall time) represents the beam exiting the active area of the photodetector and occurs in $\sim 1\text{--}2 \mu\text{s}$ (the difference between (D) and (C) labels in figure 6) however its time duration depends also on the size of the beam.

4. Signal acquisition protocol

Given the relatively small irradiance level available in the current measurement setup ($\sim 55 \text{ Wm}^{-2}$), there may be cases where the photocurrent amplitude can be close to the detection limit of the acquisition system, especially for low-performance devices. It is therefore crucial to maximize the SNR of the measurement. A new detection protocol was implemented that is based on reducing the measurement noise by acquiring the signal in a narrow window in its frequency spectrum. Similarly with a lock-in amplification technique, the aperture time for each measurement point is greatly reduced,

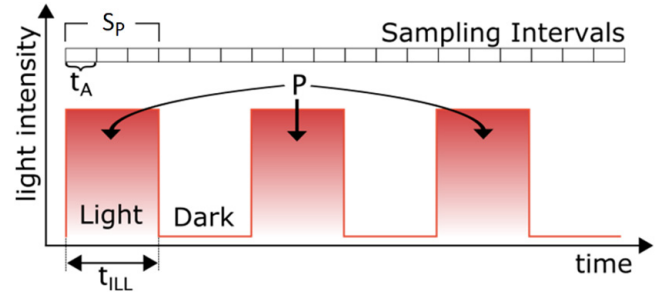


Figure 7. Description of the time-domain irradiation signal: illumination time (t_{ILL}), aperture time (t_{A}), number of pulses (P) and sample per pulse (S_{P}). Refer to the letters inside the picture.

increasing measurement speed without compromising measurement accuracy. Nevertheless, the signal modulation is provided by the DMD itself, removing the need for additional equipment for signal modulation.

4.1. Signal acquisition

All the pixels are switched on/off at a fixed modulation frequency (f_{m}) producing a square wave illumination. This is obtained by synchronous operation of all the mirrors composing a pixel and is another significant advantage when using the DMD device. The irradiation profile in the time-domain is described in figure 7. Both light and dark phases have the same time length t_{ILL} (illumination time), producing a waveform with an integer number of cycles. Each light and dark pulse contains an integer number of sampling intervals S_{P} (samples-per-pulse), with length t_{A} (aperture time). This results in an integer number of samples for every pixel to meet a coherent sampling condition so that the signal peak in the frequency spectrum always corresponds to one of the discrete Fourier transform (DFT) bins in order to minimize/cancel the spectral leakage and thus increase the accuracy of the peak amplitude. It should be noted that the current measurement device measures the average of the current across the entire aperture time (t_{A}) and that the delay between two consecutive aperture times is negligible.

The sampling frequency F_{S} is the reciprocal of the aperture time:

$$F_{\text{S}} = \frac{1}{t_{\text{A}}} \tag{1}$$

The number of samples in the frequency spectrum (N_{DFT}) is equal to half the number of samples in the time-domain, thus

$$N_{\text{DFT}} = S_{\text{P}} \cdot P \tag{2}$$

The frequency resolution is given by the ratio between the Nyquist frequency f_{N} (half the sampling frequency) and the number of DFT samples:

$$\Delta f = \frac{f_{\text{N}}}{N_{\text{DFT}}} = \frac{f_{\text{N}}}{S_{\text{P}} \cdot P} \tag{3}$$

The frequency of the main peak (modulation frequency) is therefore given by

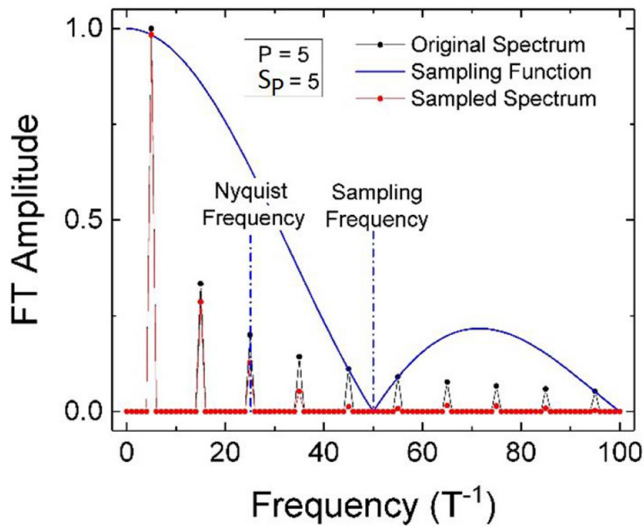


Figure 8. Simulated signal frequency spectra calculated in the case of $P = 5$ and $S_p = 5$ assuming that the system's transfer function is flat across the entire frequency range. The blue line represent the sampling spectrum due to the aperture time t_A whereas the red line represents the sampled spectrum according to the convolution theorem. The frequency axis is reported as T^{-1} (map scanning rate) because the shape of the spectrum is independent of the absolute frequency value within the bandwidth of the system.

$$f_m = \frac{1}{2t_{ILL}} = \frac{1}{2 \cdot S_p \cdot t_A} = \frac{f_N}{S_p} = \Delta f \cdot P. \quad (4)$$

It derives that within the bandwidth of the system the shape of the spectrum depends only on P and S_p , independently of the actual modulation frequency. The photocurrent can be measured by the amplitude of the main peak at the modulation frequency f_m which corresponds to the value of the $(P + 1)^{\text{th}}$ element of the DFT output array. The method has only three input parameters: t_{ILL} , S_p and P that can be quickly optimised based on the response time of the sample under test. The parameter t_{ILL} is related to the physics of the device under test: in particular, it must be set according to the response time of the device. The parameters S_p and P are instead linked to the data acquisition method.

A simulated typical spectrum for $P = 5$ and $S_p = 5$ is reported in figure 8. The acquired signal is given by the time domain convolution between the theoretical signal and the sampling function. As shown in figure 7, the sampling pattern is constituted by a train of rectangular windows with width t_A rather than a Dirac comb thus resulting in a sinc(f) shaped sampling spectrum. The small suppression of the fundamental peak is compensated for in the data analysis method.

The low-pass filter characteristic of the sampling transfer function (see figure 8) conveniently reduces the aliasing effect by suppressing the amplitude of the higher harmonics of the square wave. The simulated spectra in figure 9 show the effect of the sampling function on suppressing the aliasing contributions of 10^4 harmonics of the square wave for a $P = 5$, $S_p = 5$

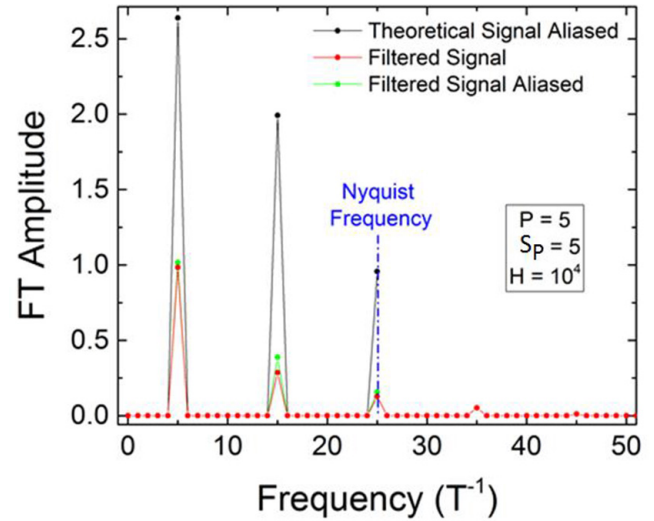


Figure 9. Comparison between the aliasing effect in the theoretical signal and the sampling filtered signal in an example spectrum with $P = 5$ and $S_p = 5$. The simulation calculates the aliasing effect of 10^4 harmonics of the square wave signal. The aliasing contribution to the fundamental frequency is significantly reduced.

spectrum. The sampled peak in the specific case increases only by 4.5% instead of a theoretical factor of 321%. This is an extreme case to show that aliasing has a very small effect on the peak's amplitude.

In fact, the number of harmonics that contribute to the peak's amplitude depends on the bandwidth of the system and therefore depends on the actual modulation frequency value f_m . However, the simulation in figure 10 reports the uncertainty as a function of the system's bandwidth for different values of S_p . In the explored range, for $S_p = 5$ the error varies from -1.64% to $+3.73\%$ whereas for $S_p = 10$ the error is within -0.42% and $+0.79\%$ across a bandwidth range 3 orders of magnitude larger than the modulation frequency. The parameter P has no effect on aliasing as it only affects the peak's frequency.

The small effect of aliasing is good because we expect to see variations in the dynamic characteristics of the device in case of specific defects, bus-bars, etc. The relative intensity of the pixels in the map is therefore preserved. Also the aliasing suppression makes the spectrum almost invariant to the actual modulation frequency thus increasing the robustness of the method.

When the modulation frequency (f_m) approaches the DMD's maximum on/off frequency limit of ~ 11.4 kHz (half the maximum frame rate) the response time of the micro mirrors shown in figure 6 starts to affect the photocurrent signal significantly. The rise time of the photocurrent ($\sim 7 \mu\text{s}$ (B) and (A) in figure 6) due to the rotation of the micro mirrors will cause the bandwidth of the system to be closer to the modulation frequency (see figure 10). As a result the higher harmonics of the square wave spectrum will be suppressed but the peak of interest will be preserved.

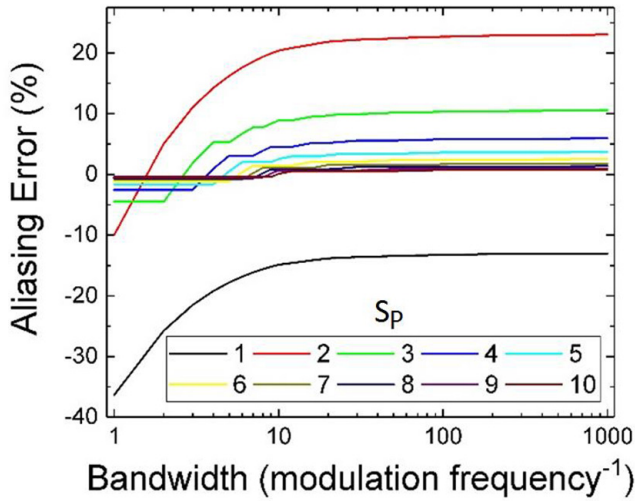


Figure 10. Aliasing error (%) as a function of the system's bandwidth for different values of S_p . The system bandwidth is reported in units of modulation frequency.

4.2. Noise measurement

The measurement of the noise level associated to each pixel in the map is necessary to determine the detection threshold of the measurement technique. The noise map can be used to obtain a quantitative estimate regarding the presence of a defect in the photocurrent map. A data processing protocol was developed to quantify the noise associated with each pixel.

If the signal was acquired without any modulation, the noise corresponding to one pixel could be determined as the standard deviation of the time-domain signal. The transient regions (rise time) of such waveform should also be discarded in the computation requiring some optimisation algorithm for each single pixel.

In the signal acquisition method described above the photocurrent at each pixel is given by the amplitude of the fundamental peak of the DFT spectrum at frequency f_m . The noise is also spectrally distributed and only a fraction falls into the peak's range resulting in a higher S/N ratio. However, it is impossible to quantify the noise component just by measuring the peak's amplitude.

The protocol devised here for this purpose is based on the assumption of linear background in the vicinity of the peak. In order for this assumption to hold, the peak must be as far away from DC as possible so that the contribution of flicker noise ($1/f$) is negligible. Given the particular combination of aperture time (t_A), illumination time (t_{ILL}) and scanning time (T) (i.e. $t_{ILL} = k \cdot t_A$ and $T = 2k' \cdot t_{ILL}$ for $k, k' \in \mathbb{N}$), the spectral leakage is minimized and the bins adjacent to the peak of interest contain only noise.

The software calculates the spectral noise power density as the mean of the power amplitude of the adjacent bins across a determined range of frequencies around the peak. In the white noise assumption the standard deviation of the modulated signal can be calculated as

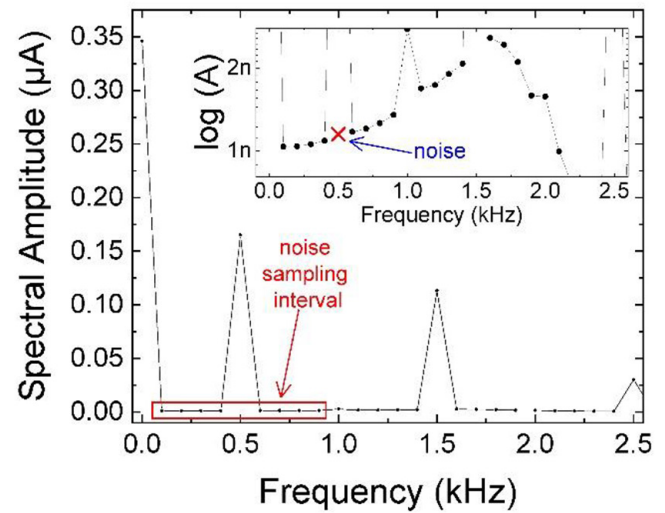


Figure 11. Analysis of the background spectral noise in an example measurement. The red square highlights the bins considered for the noise estimation. The noise level evaluated with this method is indicated by a red \times in the log scaled spectrum in the inset.

$$\sigma^2 = \frac{N_0}{2} \int_{f_p}^{f_p + \Delta f} |H(f)|^2 df \Rightarrow \sigma = \sqrt{\frac{N_0}{2T}} \quad (5)$$

where N_0 is the measured noise power density and $H(f) = 1$ is the gain.

Given the usual shape of the frequency spectra (see figure 11) the noise sampling interval chosen extends to the first bin after DC and is symmetric around the peak's frequency. The flicker noise is either very small or it decays very rapidly within one spectral resolution step. The background noise spectrum of a device can contain bands most likely due to resonance in the SMU's feedback loop and the device (see inset of figure 11). However, if the parameters are chosen correctly the mean of the adjacent bins usually represent a good estimation of the peak's background noise as shown by the red \times in inset of figure 11.

The theoretical lower bound for the noise reduction factor obtained with this method (pulsed light) compared to simply calculating the average photocurrent for each pixel with scanning frequency and sampling frequency being the same can be estimated, in the assumption of white noise, as $\sqrt{2P \cdot S_p}$.

5. Experimental results

Two copper indium gallium selenide (CIGS) photovoltaic cells with different sizes were measured. In figure 12(b), a full map of the entire cell with a lateral resolution of $137 \mu\text{m}$ (10 by 10 mirrors) was acquired in only 35 s. The scanning parameters were set to $S_p = 5$ and $P = 3$. The illumination time was set to $t_{ILL} = 1$ ms for figures 12(a) and (b) and $t_{ILL} = 5$ ms for figures 12(d) and (e). The scanning speed is mainly limited by the response speed of the device under test and by the speed of the acquisition system which depends on the current range.

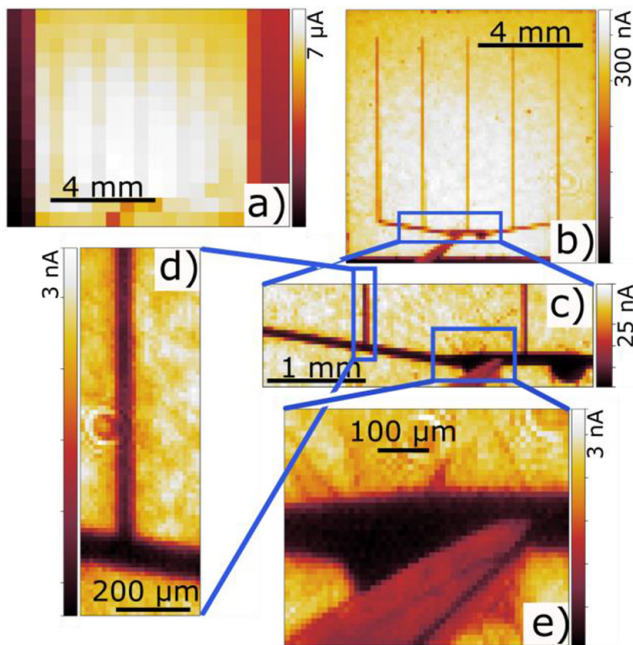


Figure 12. Mapping of a CIGS solar cell by progressively zooming-in on photocurrent features. (a) Resolution 50 mirrors, size 300 pixels and scanning time 1.8 s, (b) resolution 10 mirrors, size 5852 pixels and scanning time 35 s, (c) resolution 3 mirrors, size 2784 pixels and scanning time 16.7 s, (d) resolution 1 mirror, size 2352 pixels and scanning time 68.4 s, (e) resolution 1 mirrors, size 2279 pixels and scanning time 68.4 s. The current value next to the colour bar is the upper bound of the range whereas the lower bound is zero.

The smaller the signal amplitude the slower the acquisition speed. It is interesting to note that the cell was mapped with a scanning rate of 167 pixels per second down to a pixel size of $\sim 40 \mu\text{m}$ (3 mirrors). The scanning rate for smaller pixels size needed to be decreased to ~ 34 pixels per second to compensate for the decrease in radiated power (the irradiance is constant). This limitation can be avoided in the future if a more powerful laser is used.

The number of pixels for each scan was limited by the available RAM on the V-7000 module (4 GB) and it is not an intrinsic limit of the method. An 8 GB RAM system would allow for a full size map with $\sim 40 \mu\text{m}$ resolution and therefore no zooming in needed.

Thanks to the absence of any moving parts in the system, the mapping is highly repeatable and smaller areas can be selected from a larger field image and mapped at higher resolution.

Some of the features in the photocurrent map are zoomed in in figures 12(c)–(e) to demonstrate the achievable resolution with the current setup. The photocurrent maps have a pixel size down to a single mirror which is below the resolution limit of the optical system of $37 \mu\text{m}$ (calculated in figure 3). This contributes to the smoothing effect at the edge between high and low photocurrent areas.

In figure 13 a smaller cell is investigated. The full cell reported in figure 13(b) was scanned with a resolution of $137 \mu\text{m}$ for a total of 3402 pixels in 170 s. The scanning parameters were set to $t_{\text{ILL}} = 5 \text{ ms}$, $S_P = 5$ and $P = 5$. In order to validate the presented method, in figure 13(a) the same

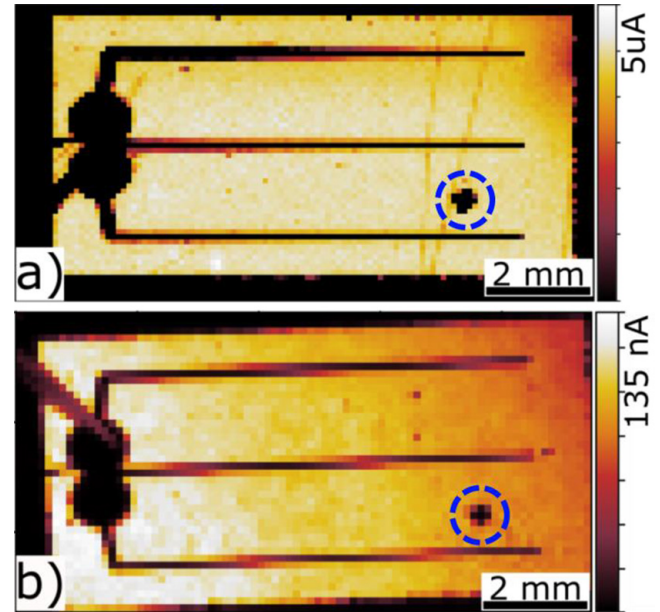


Figure 13. Mapping of a CIGS solar cell. In (a) the cell was measured using the laser beam induced current (LBIC) method with resolution 0.1 mm, size 6380 pixels and scanning time 2150 s. In (b) the cell was measured using the DMD with the method proposed here with resolution 10 mirrors, size 3402 pixels and scanning time 170 s. The current value next to the colour bar is the maximum value of the range whereas the minimum value is zero. The blue circle identifies a main point defect in both photocurrent maps.

cell was mapped with a light beam induced current (LBIC) method using a 532 nm $10 \mu\text{W}$ laser diode with a scanning rate of 3 pixel per second. Information regarding the LBIC system used is reported in [16, 17] and [18]. The LBIC image has a larger dynamic range due to the higher irradiance of the laser spot: $10 \mu\text{W}$ for the LBIC compared to $\sim 1 \mu\text{W}$ for the DMD at that particular resolution. Both methods show a similar shape for the main point defect in the bottom right region of the active area (see blue circle in both maps of figure 13). The two images also show different types of features: line defects are present in the LBIC map only, whereas some of the point defects of figure 13(a) are not detected by the LBIC. This is due to the different penetration length of the laser wavelengths used in the two measurements: longer wavelengths have deeper penetration depths. As a consequence the green laser detects mostly shallower scratches on the active area while the red laser can highlight bulk defects of the device [19]. An additional advantage of a DMD based system is that it can be wavelength invariant within the DMD's window spectral transmittance between 250 nm and $2.7 \mu\text{m}$. This could be achieved by replacing the lenses with parabolic mirrors, a fibre coupled laser source with a different wavelength can be then easily coupled to explore different types of features, without practically requiring any further modifications of the system.

6. Conclusions

A new high-speed method for measuring the photocurrent map of solar cells and photodiodes is analytically described in

this work. The integration of the optical system with the signal acquisition setup is demonstrated. The measurement system is fully characterized in terms of transient output and optical resolution capabilities.

A digital signal processing method was developed and programmatically implemented to increase the SNR and overcome the intrinsic limitations of DMD mapping where, due to the irradiance being constant, resolution and power are inversely proportional. In particular the signal acquisition method relies on the synchronization between the light field control and the photocurrent measurement. This allows the discretization of the Fourier spectrum to remove spectral leakage.

The protocol is characterized by a small number of parameters: t_{ILL} , P and S_P . This gives the method a higher flexibility and robustness as the data analysis is guaranteed to work with the same accuracy independently of scanning speed.

The spectrum discretization also enables the implementation of a simple noise quantification method which will be extremely useful for the quantitative analysis of defects and features in photocurrent maps.

Test measurements for two CIGS cells demonstrated the strengths and validity of the method and the acquired maps were validated using LBIC measurements. The data shows that the new method is much faster than when using a standard LBIC system. However, LBIC results show a higher dynamic range in the photocurrent signal especially at higher resolutions due to the fact that all the power emitted by the laser source is focused on a single pixel. This is a minor issue that can be easily overcome by integrating high power laser sources in the system, since the DMD itself can withstand up to 25 W of optical power. The addition of more powerful laser would allow further optimization of the lateral resolution and of the signal to noise ratio.

Irradiance uniformity can be remedied in a future system by adding a diffuser and then collimating the initial laser beam so that it overfills the DMD area.

The presented technique is very flexible and, thanks to the absence of any moving parts (except for the microelectromechanical parts in the DMD), allows for highly repeatable photocurrent mapping. After a quick scanning at a relatively low resolution, individual areas or features can be successively investigated without losing track of their position. This presents a huge potential for industrial automation where the recognition of defects could be implemented using a machine learning approach therefore enabling unforeseen solutions for efficient quality control processes. Thanks to the high-speed control of the light-field the protocol described here could also enable a whole plethora of innovative measurement techniques.

For example, the ability to display any possible pattern of light on a sample make this technique particularly appealing for exotic scanning protocols such as the compressed-sensing (CS) method which has proven to increase the speed and the SNR compared to the common raster scanning method. The high-speed of the measurement protocols presented here combined with CS is therefore a very promising field for further investigation.

The system can also be easily scaled up for mapping larger area devices up to the size of standard solar panels (1×1.7 m) by replacing the collimated optics with projection optics. This can be combined with a higher power laser source, the implementation of compressed sensing mapping algorithms and the illumination modulation signal acquisition protocol presented in this work in order to maximize the SNR.

Acknowledgments

The work was funded by the Department for Business, Energy and Industrial Strategy (BEIS) through the National Measurement System and by the EMPIR project PVenerate. The EMPIR initiative is co-funded by the European Union's Horizon 2020 research and innovation programme and the EMPIR Participating States. Authors thank Dr Stephan Brunken (HZB) for kindly providing CIGS samples used in this work.

ORCID iDs

George Koutsourakis  <https://orcid.org/0000-0002-5552-1749>

James C Blakesley  <https://orcid.org/0000-0002-7027-4918>

Fernando A Castro  <https://orcid.org/0000-0002-2409-8300>

References

- [1] Schuss C *et al* 2016 Detecting defects in photovoltaic cells and panels and evaluating the impact on output performances *IEEE Trans. Instrum. Meas.* **65** 1108–19
- [2] Redfern D A, Musca C A, Dell J M and Faraone L 2005 Characterization of electrically active defects in photovoltaic detector arrays using laser beam-induced current *IEEE Trans. Electron Devices* **52** 2163–74
- [3] Padilla M, Michl B, Thaidigsmann B, Warta W and Schubert M C 2014 Short-circuit current density mapping for solar cells *Sol. Energy Mater. Sol. Cells* **120** 282–8
- [4] Redfern D A, Smith E P G, Musca C A, Dell J M and Faraone L 2006 Interpretation of current flow in photodiode structures using laser beam-induced current for characterization and diagnostics *IEEE Trans. Electron Devices* **53** 23–31
- [5] Bokalic M, Jankovec M and Topic M 2009 *45th Int. Conf. on Microelectronics, Devices and Materials & The Workshop on Advanced Photovoltaic Devices and Technologies* pp 269–73
- [6] Thantsha N M, Macabebe E Q B, Vorster F J and van Dyk E E 2009 Opto-electronic analysis of silicon solar cells by LBIC investigations and current–voltage characterization *Physica B* **404** 4445–8
- [7] Carstensen J, Popkirov G, Bahr J and Föll H 2003 CELLO: an advanced LBIC measurement technique for solar cell local characterization *Sol. Energy Mater. Sol. Cells* **76** 599–611
- [8] Vorasayan P, Betts T R, Tiwari A N and Gottschalg R 2009 Multi-laser LBIC system for thin film PV module characterisation *Sol. Energy Mater. Sol. Cells* **93** 917–21
- [9] Geishardt R M and Sites J R 2014 Nonuniformity Characterization of CdTe Solar Cells Using LBIC *IEEE J. Photovolt.* **4** 1114–8
- [10] Hornbeck L J 2001 The DMD™ projection display chip: a MEMS-based technology *MRS Bull.* **26** 325–7

- [11] Hall S R G, Cashmore M, Blackburn J, Koutsourakis G and Gottschalg R 2016 Compressive current response mapping of photovoltaic devices using MEMS mirror arrays *IEEE Trans. Instrum. Meas.* **65** 1945–50
- [12] Koutsourakis G, Cashmore M, Hall S R G, Bliss M, Betts T R and Gottschalg R 2017 Compressed sensing current mapping spatial characterization of photovoltaic devices *IEEE J. Photovolt.* **7** 486–92
- [13] Quan L, Xie K, Liu Y and Zhang H 2019 Camera enhanced compressive light beam induced current sensing for efficient defect detection in photovoltaic cells *Sol. Energy* **183** 212–7
- [14] Koutsourakis G, Cashmore M, Bliss M, Hall S R G, Betts T R and Gottschalg R 2016 Compressed sensing current mapping methods for PV characterisation *Conf. Record of the IEEE Photovoltaic Specialists Conf.* vol 2016–Novem pp 1308–12
- [15] Rice J P, Neira J E, Kehoe M and Swanson R 2009 *Proc. SPIE* **7210** 72100D
- [16] Kutsarov D I, New E, Bausi F, Zoladek-Lemanczyk A, Castro F A and Silva S R P 2017 Fabrication of air-stable, large-area, PCDTBT:PC₇₀BM polymer solar cell modules using a custom built slot-die coater *Sol. Energy Mater. Sol. Cells* **161** 388–96
- [17] Kylberg W *et al* 2013 Spatially resolved photocurrent mapping of efficient organic solar cells fabricated on a woven mesh electrode *Prog. Photovolt., Res. Appl.* **21** 652–7
- [18] Risbridger T A G, Castro F A and Cameron P J 2012 Two-dimensional photocurrent and transmission mapping of aqueous dye-sensitized solar cells *J. Phys. Chem. C* **116** 22253–60
- [19] Brooks W S M, Irvine S J C and Barrioz V 2011 High-resolution laser beam induced current measurements on Cd_{0.9}Zn_{0.1}S/CdTe solar cells *Energy Proc.* **10** 232–7